# The depth of Jupiter's Great Red Spot constrained by the Juno gravity overflights

Marzia Parisi, Yohai Kaspi, Eli Galanti, Daniele Durante, Scott J Bolton, Steven M Levin, Dustin R Buccino, Leigh N Fletcher, William M Folkner, Tristan Guillot, et al.

# The depth of Jupiter's Great Red Spot constrained by the Juno gravity overflights

Marzia Parisi,[1*] Yohai Kaspi,[2] Eli Galanti,[2] Daniele Durante,[3] Scott J. Bolton,[4] Steven M. Levin,[1] Dustin R. Buccino,[1] Leigh N. Fletcher,[5] William M. Folkner,[1] Tristan Guillot,[6] Ravit Helled,[7] Luciano Iess,[3] Cheng Li,[8] Kamal Oudrhiri,[1] Michael H. Wong,[9,10]

[1]Jet Propulsion Laboratory, California Institute of Technology, Pasadena, CA 91109, USA

[2]Department of Earth and Planetary Sciences, Weizmann Institute of Science, Rehovot 76100, Israel

[3]Department of Mechanical and Aerospace Engineering, Sapienza University of Rome, Rome 00184, Italy

[4]Southwest Research Institute, San Antonio, TX 78238, USA

[5]Department of Physics and Astronomy, University of Leicester, Leicester LE1 7RH, United Kingdom

[6]Université Côte d'Azur, Observatoire de la Côte d'Azur, Laboratoire Lagrange du Centre National de la Recherche Scientifique, 06304 Nice, France

[7]Center for Theoretical Astrophysics & Cosmology, Institute for Computational Science, University of Zurich, 8057 Zurich, Switzerland

[8]Department of Climate and Space Sciences and Engineering, University of Michigan, Ann Arbor, MI 48109, USA

[9]Department of Astronomy, University of California Berkeley, Berkeley, CA 94720, USA

[10]Search for Extraterrestrial Intelligence Institute, Mountain View, CA 94043, USA

[*]To whom correspondence should be addressed; E-mail: marzia.parisi@jpl.nasa.gov

**Jupiter's Great Red Spot (GRS) - the largest and most iconic vortex in the Solar System - has been observed for at least two centuries.**

**A key question is how deep the vortex extends beneath its visible clouds. Here, we examine the gravity signature of the GRS using data from twelve encounters of the Juno spacecraft with the planet, including two direct overflights of the vortex. We identify localized density anomalies due to the presence of the GRS, which cause a shift in the spacecraft line-of-sight velocity. Using two different approaches to infer the GRS depth, both yielding consistent results, we find that the GRS is contained in the upper 500 km of Jupiter's atmosphere, and is 300±100 km deep at the 1$\sigma$ level.**

# Main text

Jupiter's Great Red Spot (GRS) is a large anticyclonic storm in Jupiter's atmosphere. The combination of its size (more than 16,000 km east-west) and longevity make it unique in the Solar System, and are related to the underlying dynamics of the storm. A key question has been whether the vortex needs to be deep-rooted in the surrounding zonal flows in order to sustain its structure, or whether a shallow system can support such a long-living storm (*1, 2*). The Juno gravity measurements are sensitive to density perturbations in the deeper layers of the atmosphere, below the visible cloud level, and close encounters with the vortex can be exploited to study its gravity signature and infer the depth of its winds.

The Juno spacecraft flew twice over the GRS at altitudes <20,000 km, in February and July 2019. These encounters (perijoves) were dedicated to measurements of the local gravitational field. Earlier observations of the GRS had occurred in July 2017, during which the spacecraft attitude was optimized for Microwave Radiometer (MWR) investigations, precluding gravity measurements. The microwave observations indicated that the GRS extended down to at least a hundred bars below the cloud level (estimated at

0.7 bar), corresponding to a depth of ∼240 km (*3, 4*). MWR observations are complementary to gravity measurements as they provide a minimum value for the vortex's vertical extension (*3*), and an insight into its internal structure and dynamics (*4*). Juno gravity measurements revealed Jupiter's gravity field is hemispherically asymmetric (*5*), whose existence has been explained by the powerful zonal winds in which the GRS is embedded (*6*). The depth of the jet-streams has been estimated at 3,000 km by relating the observed cloud-level winds to the gravity measurements via thermal wind balance, which is the governing vorticity balance on large, rapidly rotating planets (*7*). However, it remains unclear how far down the GRS winds extend between the surrounding jet-streams.

Using gravity data to determine the depth of the GRS was proposed before Juno's arrival at Jupiter (*8*), by determining the planet's longitudinally-dependent gravity field. Alternatively, the use of a Slepian basis has been proposed (*9*), whose functions are defined as linear combinations of spherical harmonic functions, capable of maximizing the amount of information in a chosen domain. This approach has previously been used to describe localized features on Earth (*10, 11*) and when using data collected over a limited area (*12*). Those simulations predicted that the gravity signal of the GRS could potentially be described with a single Slepian coefficient and that the gravity data would be sensitive to the depth of the GRS if it was at least a few hundred kilometers (*9*). Similar conclusions were reached using a complementary approach that models the GRS as a vertical dipole of mass concentrations (mascons), in which the mass of the anomalies is estimated directly (*13*).

Juno's orbit around Jupiter is quasi-polar and highly eccentric, with the spacecraft descending to altitudes of about 3,500 km over Jupiter's cloud tops every 53 days, sweeping the planet from its north to south pole within a couple of hours (*14*). The oblateness of the planet causes a northward shift of the perijove latitude of ∼1° per orbit from an initial

latitude of 4°N. Therefore the spacecraft observes the GRS (20°S) from an increasing distance as the mission proceeds. During gravity passes, two-way Doppler measurements of the spacecraft range-rate were performed using coherent radio links with NASA's Deep Space Network in X- (≈8 GHz) and Ka-band (≈32 GHz) (*15*), which are sensitive to perturbations in the gravity field of Jupiter. We analyze data from twelve Juno perijoves (PJs) labeled with progressive numbers 1, 3, 6, 8, 10, 11, 13, 14, 15, 17, 18 and 21. We initialize Jupiter's global gravity field and tidal response using Juno gravity data up to PJ17 (*16*), to these we add the GRS overflights data from PJ18 and PJ21. Figure 1 shows the Juno tracks over Jupiter's reference surface during the latter passes.

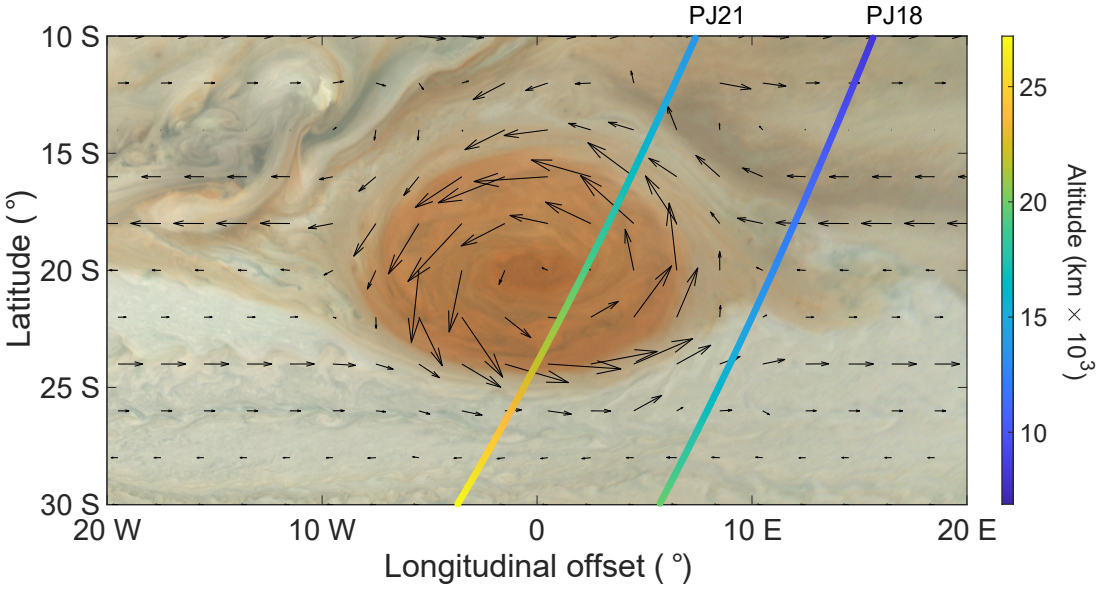


Figure 1: **Geometry of the Juno GRS gravity observations**. The GRS velocity field (black arrows) at the time of Juno's PJ21 (*17*) and Juno tracks during PJ18 and PJ21 (cyan and green lines), superimposed on JunoCam imaging of the GRS collected between PJ7 and PJ21 (*18*). The spacecraft altitude during the GRS closest approach was 13,000 km and 19,000 km, with eastward longitudinal offsets of 11° and 2°, during PJ18 and PJ21, respectively.

We combine the Juno gravity measurements using a least-squares multiarc filter implemented in the orbit determination software MONTE (*19*), which was also used for

trajectory integration and data analysis. The range-rate integration time was 60 seconds and the typical noise Root Mean Square (RMS) was between 5 and 10 $\mu\,\mathrm{ms}^{-1}$ (one-way). The filter requires the accurate reconstruction of the Juno trajectory, including every acceleration acting on the spacecraft, gravitational and non-gravitational (*5, 16*). We searched for the GRS gravity signature in the Juno overflight data by processing the range-rate residuals while solving for the zonal gravity field of Jupiter. Previous analyses (*16*) have discussed the difficulty of fitting the Juno range-rate data from multiple perijoves without allowing for longitudinal or temporal variations of the gravity field.

The range-rate residuals for PJ18 and PJ21, after removing the effect of the zonal gravity field, show non-negligible signals over time scales of $\pm 1$ h around closest approach to Jupiter (fig. 2A,C). These deviations from zonal symmetry can be removed by the addition of short-lasting, constant accelerations (*16*), but could also be partly attributed to the GRS. While the closest approaches to Jupiter occurred at latitudes around 20°N, Juno crossed the GRS latitude 20°S about 20 minutes later. We analyze the remaining non-axially symmetric, non-static signatures on the range-rate residuals after removing the effect of the zonal gravity field of Jupiter. Our objective is to isolate the longitudinal or temporal effects, which include the signal from the GRS.

The measured PJ18 residuals (fig. 2A) show deviations from the mean value about 10 minutes before perijove (latitude ∼30°N). We do not expect these fluctuations to be related to the GRS, as the spacecraft was ∼100,000 km away. Figure 2A also shows the expected gravity signal from the GRS, assuming that the cloud-level winds decay at a depth $H$. The correlation between the predicted GRS signature and the smoothed residuals is shown in fig. 2D.

PJ21 data (fig. 2C) also show correlation with the GRS signal, with a constant shift in the line-of-sight velocity of about 5 $\mu\,\mathrm{ms}^{-1}$, lasting until at least 1.5 h after perijove. This

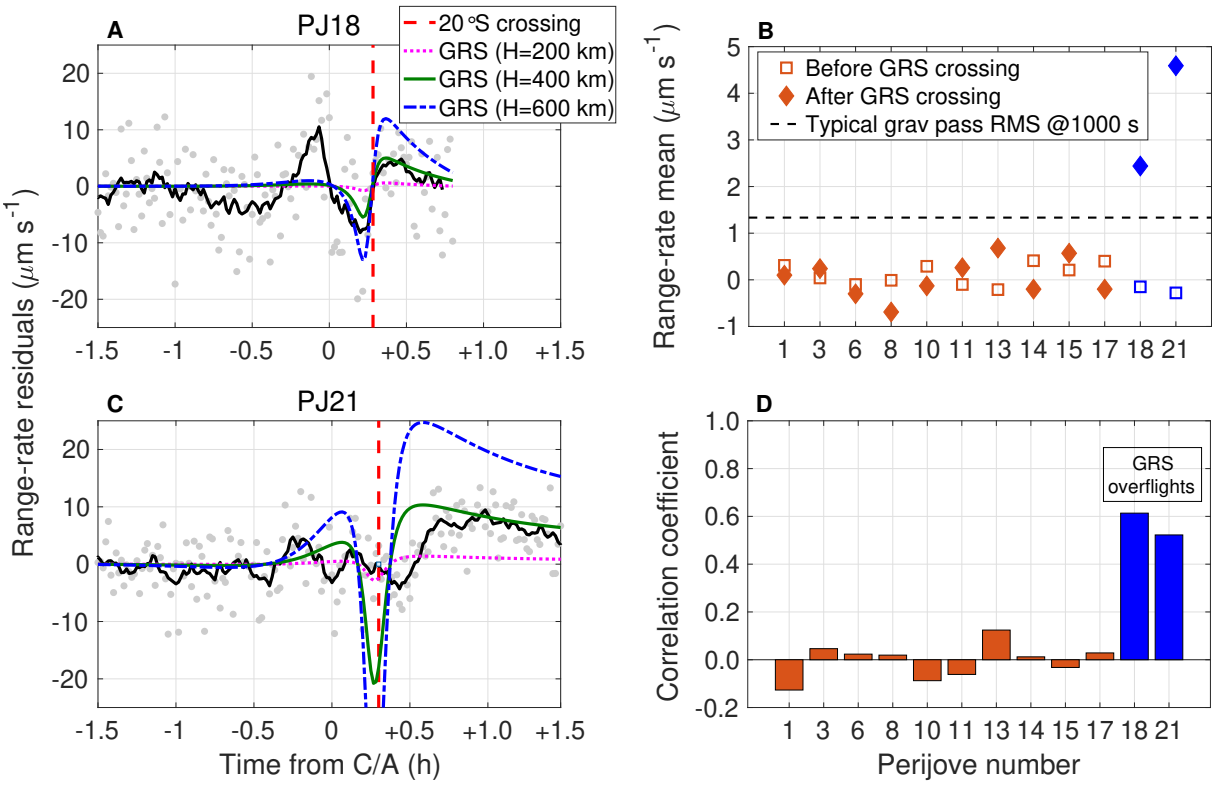


Figure 2: **Non-zonal, non-static effects on the range-rate residuals from PJ18 and PJ21**. (A and C) PJ18 and PJ21 range-rate residuals (grey dots) and their 10-minute moving average (black solid line), for the period ±1.5 h around closest approach to Jupiter (C/A). The red dashed vertical line marks the time of the GRS crossing (20°S) by the spacecraft track. The colored lines, characterized by different styles, represent the expected gravity signal from the GRS for different depths. (B) The range-rate mean values ($\Delta v$), before (squares) and after (diamonds) the crossing of latitude 20°S, for all perijoves with gravity measurements. (D) The correlation coefficients between the predicted GRS gravity signal ($H$=300 km) and the moving average of the residuals. In C and D, orange represents the non-GRS perijoves, while blue represents the GRS overflights.

behavior is typical of passing one or more mass concentrations, such as those associated to the GRS. The long duration of the constant shift favors decoupling of the constant accelerations applied around perijove from the GRS signal. We interpret the temporal offset between the negative peaks around the GRS crossing (measured versus predicted), as due to unrelated non-zonal effects. In (*20*), we discuss the role of the accelerations in

removing the excess longitudinal and/or temporal signatures and aliasing with the GRS parameters. After compensating for the estimated accelerations (fig. S7C,D), we find that: (i) most of the remaining range-rate signal can be explained by concentrated masses at the GRS location; (ii) unexplained non-zonal effects (*16*) can cause the offset between the PJ21 range-rate residuals and the predicted GRS signal (fig. 2C).

The average velocity shift ($\Delta v$) in the residuals before and after the crossing of latitude 20°S, for all perijoves, is shown in fig. 2B. These averages are calculated over time periods of 0.5-1.5 h. Passes over the GRS show shifts of a few $\mu$ ms$^{-1}$, above the typical noise RMS for integration times >1000 s (*20*). Conversely, the velocity profiles for perijoves away from the GRS do not show deviations from the mean. The magnitude of the offset on the range-rate data contains direct information on the GRS depth (*20*), that is reflected in the output parameters of the least-squares solution that are used to infer the vertical extent of the winds.

Figure 2D shows the correlation coefficients between the predicted GRS gravity signal for $H$=300 km and the moving average of the range-rate residuals, for all 12 perijoves (*20*). The non-GRS passes are characterized by very low correlations of less than 10%, while the correlations for PJ18 and PJ21 are 50-60%. Despite the low signal-to-noise-ratio, perijoves 18 and 21 differ from the other passes, indicating that the GRS depth can be constrained using the Juno gravity data.

The shape of the GRS has evolved over the past several decades, with its longitudinal dimension shrinking and giving the vortex a more circular shape (*21, 22*). We measured horizontal wind speeds in the GRS using optical data acquired about 25 days prior to Juno's PJ21 (*20*), as part of an annual Hubble Space Telescope observing program (*23*). Mean velocities measured in the high-speed ring are 106 m s$^{-1}$, with a standard deviation of 11 m s$^{-1}$. Despite the wealth of information about the surface dynamics of the zonal

winds and the vortex, little is known about the dynamics below the cloud level. The surrounding jets extend very deep (*7*), which confines the latitudinal extent and direction of the GRS circulation. We therefore assume the vortex preserves its shape until it decays below the depth $H$. For simplicity we consider a hyperbolic tangent decay function, assumed to decay rather sharply within 100 km around $H$ (*25, 26*), but our results are robust to other decay shapes (*20*). Because the planet is rapidly rotating, and the dynamics are to leading order geostrophic, thermal wind balance can be used to calculate the density anomalies balancing the vortex (*24*). The applicability of this approach to modeling Jupiter's atmosphere has been extensively discussed elsewhere (*27, 28*). Unlike Earth's atmospheric vortices (*29*), the local centripetal force can be neglected.

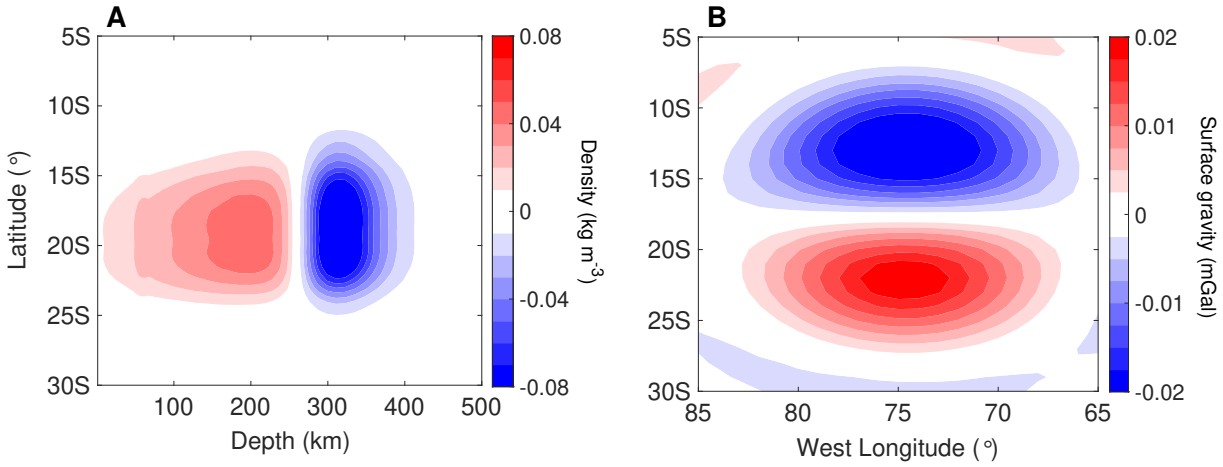


Figure 3: **The predicted signal of a 300 km deep GRS, based on thermal wind balance**. (A) Density anomalies as a function of depth and latitude, for a transversal section taken at the longitude passing through the GRS center at the time of the velocity measurements (*20*). (B) Surface gravity anomalies as a function of longitude and latitude.

The predicted density anomalies associated with the GRS for a sample depth $H$=300 km are shown in fig. 3A. The density profile resembles a dipole, with a positive mascon mass, labeled as $GM_A$ (where $G$ is the gravitational constant), in the upper levels and a negative mass ($GM_B$) at depth. The sum of the two masses is zero, to first order (*20*).

The relationship between the mass and the separation between the positive and negative anomaly is injective (fig. S3), therefore the depth ($H$) can be inferred from estimating the mass using MONTE (*13*). In the orbit determination software, we model the vortex as a pair of flat disk mascons, whose masses are constrained to be equal and opposite in sign. Deeper winds entail a larger mass involved in the circulation of the GRS and an increasing vertical distance between the mascons. A sign inversion between the upper and deeper levels was also observed in MWR measurements during Juno's seventh perijove (*3*).

An alternative approach to searching for the GRS gravity signature is to employ Slepian functions to characterize the wind-induced, concentrated surface gravity anomalies (*9*). Figure 3B shows the GRS predicted gravity disturbances form a north-south dipole. The Slepian functions are defined within the bounded domain delimited by an ellipsoid centered at the GRS location and spanning 20° in latitude and 30° in longitude. Our analysis of the Slepian functions (*20*) shows that a single function, labeled $\boldsymbol{g_2}$, can describe the gravity perturbations generated by the GRS, to leading order (*9*). The magnitude of the corresponding Slepian coefficient $\alpha_2$ increases with the depth of the GRS (fig. 4) and therefore, the depth ($H$) can be inferred from $\alpha_2$.

To account for unmodeled accelerations (fig. 2A,C), we introduce small constant accelerations each of 10 minute duration, for ±1 h around perijove (*16, 30*). In addition to standard estimated parameters, such as Jupiter's zonal gravity field and pole position (*20*), we also add one coefficient specific to the determination of the depth of the GRS: the gravitational parameter of the positive disk mascon $GM_A$, for the mascon approach; or the Slepian coefficient $\alpha_2$, for the Slepian approach. Both parameters are unconstrained.

The results of the mascon analysis are shown in fig. 4A. The dipole structure is implemented in MONTE and the vertical separation affects both the estimated central value of $GM_A$ and its formal uncertainty (*13*). We measure $GM_A = (1.47 \pm 1.08) \times 10^{-1}$ km$^3$s$^{-2}$.

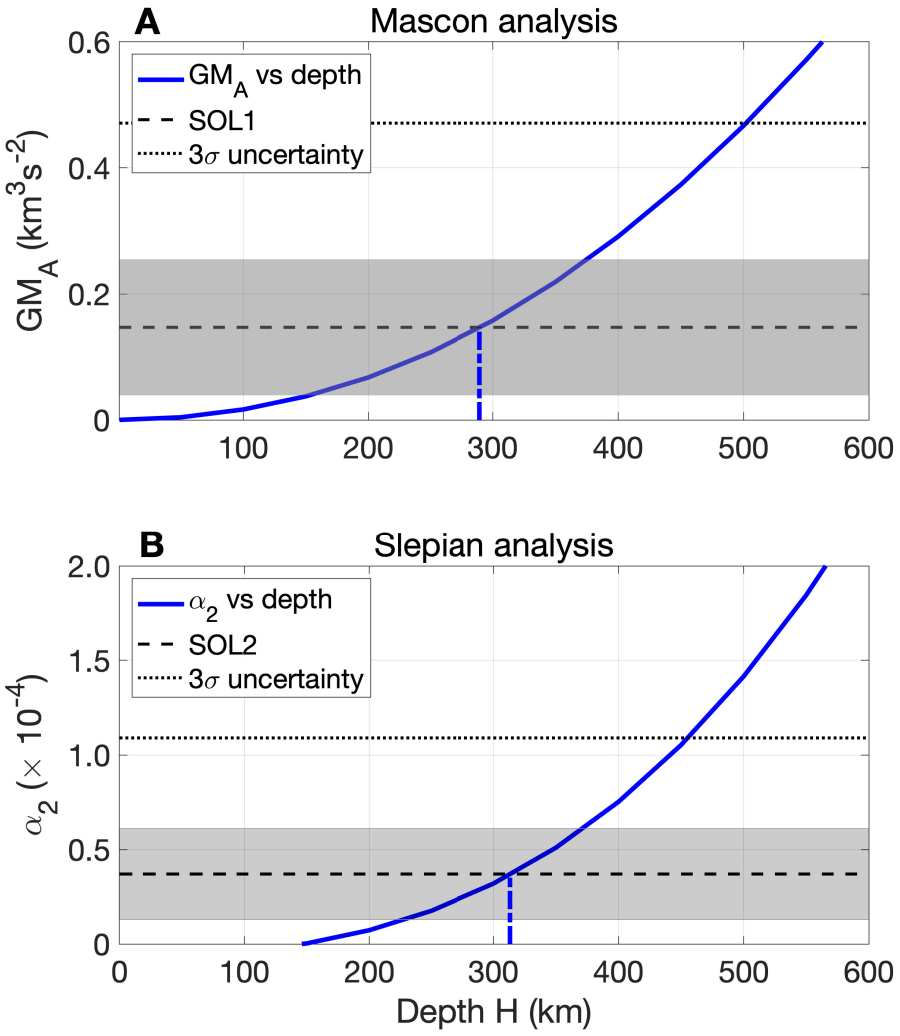


Figure 4: **Results of the GRS depth estimation**. (A) Results of the mascon approach (SOL1), with the $H$ and $GM_A$ relationship from thermal wind balance (blue). (B) Results of the Slepian approach (SOL2) and the $H$ and $\alpha_2$ relationship for the predicted gravity anomalies (blue). For both analyses, the estimated value from the Juno measurements is also shown, with the $1\sigma$ uncertainty (gray shaded area) and the $3\sigma$ level (dotted).

The derived GRS depth is then obtained from the predicted $H$ and $GM_A$ relationship from thermal wind. We find $H = 290^{+85}_{-140}$ km, which is fully compatible with the Juno MWR observations (*4*). For the Slepian approach (fig. 4B), the estimated $\alpha_2$ coefficient

is $(3.7 \pm 2.4)\times10^{-5}$, which implies the winds extend down to $H = 310^{+60}_{-90}$ km. All uncertainties are given at $1\sigma$. Thus, the two different methods give compatible solutions for the depth of the GRS. We tested the stability of both solutions against different models of the unknown non-zonal, non-static effects, which support the robustness of the estimated depth (*20*).

Both methods assume the GRS is in thermal wind balance, and each has strengths and limitations, which are complementary to one another (*13, 20*). However, they differ in the way the predicted density profile is used: either to model mass concentrations or to model the gravitational potential at the spacecraft altitude. They provide consistent results and indicate that with $3\sigma$ accuracy (fig. 4), the GRS is no deeper than 500 km (750 bar). This upper limit is compatible with laboratory analogue experiments and numerical simulations (*31, 32*). At the $1\sigma$ uncertainty, we find the GRS is 300±100 km deep. However, the minimum depth of the GRS is not strongly constrained. This was expected because the GRS gravity signal is about 20 times weaker than the background zonal wind signal (*5, 16*). Our use of random accelerations de-weights the Doppler data and increases the formal uncertainties. Juno MWR observations provide a minimum value for the vortex's vertical extension of approximately 240 km (*3, 4*), which complement our gravity measurements. While it is possible that the GRS winds still increase below the cloud level (*33*), before they begin decaying deeper down, any increase must be less than 50% of the cloud-level velocity, otherwise the inferred depth would be shallower than indicated by MWR. We therefore conclude that the depth of the GRS is between 200 and 500 km.

Our results suggest that the GRS is much shallower than the surrounding zonal jets, which have depths of around 3,000 km (*7*), but is deeply rooted far below the cloud-level at 0.7 bar and well beyond the water condensation level (∼80 km beneath the

cloud level) (*33*). The GRS is still overall shallow in terms of the aspect ratio between the vertical and horizontal scales ($\sim$1/200 or 0.5%). This is even shallower than Earth cyclones and anticyclones, which have typical ratios of 1-4%, though they are limited by the depth of Earth's troposphere. Moreover, the driving mechanisms for Earth's vortices are very different, with an important role played by solid surfaces, not present on Jupiter. It remains unclear why the GRS has a depth of 300 km while the surrounding jets, which power the GRS, extend much deeper. However a relatively shallow GRS is consistent with its change in size over several decades (*22*).

# References


1. T. E. Dowling, A.P. Ingersoll, *J. Atmos. Sci.*, **46**(21), 3256-3278 (1988).

2. J. Yano, G. R. Flierl, *Ann. Geophys.*, **12**(1), 1-18 (1994).

3. S. J. Bolton et al., Submitted with this paper (2021).

4. C. Li et al., Submitted with this paper (2021).

5. L. Iess et al., *Nature*, **555**, 220-222 (2018).

6. Y. Kaspi, *Geophys. Res. Lett.*, **40**(4), 676-680 (2013).

7. Y. Kaspi et al., *Nature*, **555**, 223-226 (2018).

8. M. Parisi, E. Galanti, S. Finocchiaro, L. Iess, Y. Kaspi, *Icarus*, **267**, 232-242 (2016).

9. E. Galanti et al., *Astrophys. J.*, **874**(2), L24 (2019).

10. C. Harig, F.J. Simons, *Proc. Natl. Acad. Sci.*, **109**, 49, 19934-19937 (2012).

11. F. J. Simons, F. A. Dahlen, M. A. Wieczorek, *SIAM Rev.*, **48**(3), 504-536 (2006).

12. F. J. Simons, F. A. Dahlen, *Geophys. J. Int.*, **166**(3), 1039-1061 (2006).

13. M. Parisi et al., *Planet. Space Sci.*, **181**, 104781 (2020).

14. S. J. Bolton et al., *Science*, **356**(6340), 821-825 (2017).

15. S. W. Asmar et al., *Space Sci. Rev.*, **213**, 205-218 (2017).

16. D. Durante et al., *Geophys. Res. Lett.*, **47**(4) (2020).

17. https://doi.org/10.17909/t9-jfs3-p240

18. Credit: Enhanced image by Björn Jónsson (CC-NC-SA) based on images provided courtesy of NASA/JPL-Caltech/SwRI/MSSS. Citizen scientist Björn Jónsson created this montage using JunoCam data, available at: https://www.jpl.nasa.gov/images/a-storm-of-change, under the Creative Commons Attribution-NonCommercial-ShareAlike 2.0 license (https://creativecommons.org/licenses/by-nc-sa/2.0/legalcode)

19. S. Evans et al., *CEAS Space J.*, **10**(1), 79–86 (2018).

20. Materials and methods are available as supplementary materials.

21. A. A. Simon et al., *Astron. J.*, **155**(4), 151 (2018).

22. A. Sànchez-Lavega et al., *Astron. J.*, **156**(4), 162 (2018).

23. A. A. Simon, M.H. Wong, G. Orton *Astrophys. J.*, **812**(1), 55, (2015).

24. Y. Kaspi, W. B. Hubbard, A. P. Showman, G. R. Flierl, *Geophys. Res. Lett.*, **37**(1), L01204 (2010).

25. E. Galanti et al., *Geophys. Res. Lett.*, **46**(2), 616–624 (2019).

26. Y. Kaspi et al., *Space Sci. Rev.*, **216**, 5, 84 (2020).

27. K. Zhang, D. Kong, G. Schubert, *Astrophys. J.*, **806**(2), 270 (2015).

28. E. Galanti, Y. Kaspi, E Tziperman, *J. Fluid. Mech.*, **810**, 175-195 (2017).

29. J. R. Holton, *An Introduction to Dynamic Meteorology* (Burlington, MA: Elsevier Academic Press, 2004).

30. L. Iess et al., *Science*, **364**, 6445 (2019).

31. D. Lemasquerier et al., *Nature Phys.*, **16**, 695–700 (2020).

32. R. K. Yadav, M. Heimpel, J. Bloxham, *Sci. Adv.*, **6**, 46 (2020).

33. L.N. Fletcher et al., *Icarus*, **208**(1), 306-328 (2010).

34. L. Dressel, *Wide Field Camera 3 Instrument Handbook, Version 13.0* (Baltimore: STScI, 2021).

35. M.H. Wong et al., *Astrophys. J., Suppl. Ser.*, **247**, 58 (2020).

36. X.S. Asay-Davis, P.S. Marcus, M.H. Wong, I. de Pater, *Icarus*, **203**(1), 164-188 (2009).

# Acknowledgments

We thank David J. Stevenson, Andrew P. Ingersoll, the Juno Interiors and Atmospheric Working Groups for useful discussions. We thank citizen scientist Björn Jónsson, who processed the background image in fig. 1 as part of Juno's JunoCam outreach program.

We thank Nimrod Gavriel for helping with the graphics of fig. 1. **Funding:** This research was carried out at the Jet Propulsion Laboratory, California Institute of Technology (MP, SML, DRB, WMF, KO), under contract number 80NM0018D0004 with the National Aeronautics and Space Administration (NASA); at the Weizmann Institute of Science (WIS) in Israel (EG and YK) with support from the Israeli Space Agency and the Helen Kimmel center for Planetary Science at WIS; at Sapienza University of Rome (DD and LI) under contract number 2017-40-H.0 with the Italian Space Agency (ASI); at the Southwest Research Institute (SJB) under contract to National Aeronautics and Space Administration; at the University of Leicester (LNF) with support by a European Research Council Consolidator Grant (under the European Union's Horizon 2020 research and innovation programme, grant agreement No 723890); at the Observatoire de la Côte d'Azur (TG) under the sponsorship of the Centre National d'Etudes Spatiales; at UC Berkeley and the SETI Institute (MHW) with support from NASA through Participating Scientist grant number 80NSSC19K1265 and through the Space Telescope Science Institute (for programs GO-13937 and GO-15502), which is operated by the Association of Universities for Research in Astronomy, Inc., under NASA contract NAS 5-26555; CL was supported by the 51 Pegasi b Postdoc Fellowship sponsored by the Heising-Simons Foundation. **Author contributions:** MP led the data analysis and interpretation of the gravity data. MP, YK and EG wrote the manuscript. YK proposed the idea for this study and assisted in the interpretation of the results. EG performed the thermal wind analysis and EG an DD performed the Slepian approach calculations. DRB, WMF and KO assisted with the data collection, processing and analysis. SJB, SML, LNF, TG, RH, LI, CL assisted with the interpretation of the results. MHW contributed the acquisition of the Hubble observations as well as performing the data analysis for the retrieval of the GRS velocity profile.

**Competing interests:** We declare no competing interests.

**Data and materials availability:** The Juno gravity data used for this analysis, from 2016 Day of Year (DOY) 240 to 2019 DOY 202, are available through NASA's Planetary Data System at https://atmos.nmsu.edu/PDS/data/jnogrv_1001//DATA/RSR/. The geometry of the Juno orbit for the time period considered in this analysis (2016-2019), including SPK for trajectory files ans CK for spacecraft attitude files, is available at https://naif.jpl.nasa.gov/pub/naif/JUNO/kernels/. The raw imaging data from the Hubble Space Telescope (IDs: iduy09mmq; iduy09mvq; iduy10n4q; iduy15ooq) are available from the MAST archive (https://archive.stsci.edu/hst/search.php), by searching program GO-15502. The velocity field is available as a HDF5-format dataset on the MAST archive at https://doi.org/10.17909/t9-jfs3-p240. Distribution of the MONTE navigation code is restricted by the Export Administration Regulations of the US Department of Commerce. Eligible readers may request a copy of MONTE, under a license which does not permit redistribution at https://montepy.jpl.nasa.gov/. The range-rate residuals for PJ1 to PJ21 and partial derivatives for sample GRS parameters are available at https://doi.org/10.5281/zenodo.4649459. Executable code for running the thermal wind model is available at: https://github.com/egalanti/TW_GRS_Slepians (requires MATLAB).

# Supplementary materials

Materials and Methods

Figures S1-S9

Tables S1-S3

References (34-36)